

# Electrically induced strong modulation of magnons transport in ultrathin magnetic insulator films

J. Liu, X-Y. Wei,<sup>\*</sup> and B. J. van Wees<sup>†</sup>

*Physics of Nanodevices, Zernike Institute for Advanced Materials,  
University of Groningen, Nijenborgh 4, 9747 AG Groningen, The Netherlands*

G. E. W. Bauer

*Zernike Institute for Advanced Materials, University of Groningen,  
Nijenborgh 4, 9747 AG Groningen, The Netherlands and  
WPI-AIMR & Institute for Materials Research & CSRN, Tohoku University, Sendai 980-8577, Japan*

J. Ben Youssef

*LabSTICC, UMR CNRS 6285, Université de Bretagne Occidentale,  
6 Avenue Le Gorgeu, 29238 Brest Cedex 3, France*

(Dated: November 17, 2020)

Magnon transport through a magnetic insulator can be controlled by current-biased heavy-metal gates that modulate the magnon conductivity via the magnon density. Here, we report nonlinear modulation effects in 10 nm thick yttrium iron garnet (YIG) films. The modulation efficiency is larger than 40%/mA. The spin transport signal at high DC current density ( $2.2 \times 10^{11}$  A/m<sup>2</sup>) saturates for a 400 nm wide Pt gate, which indicates that even at high current levels a magnetic instability cannot be reached in spite of the high magnetic quality of the films.

## I. INTRODUCTION

Magnons, i.e. the quanta of spin waves, are carriers of information with properties that are attractive for applications [1]. Magnons propagate in ferro-, ferri, antiferro-, and even paramagnetic electric insulators without Joule heating [2–5]. The ferrimagnet yttrium iron garnet (YIG) is to date the best platform for magnon spintronics due to its low Gilbert damping and high Curie temperature. In YIG, magnons can be excited thermally and electrically and can cover long distances [6–8]. An electric current  $I$  in a thin-film platinum contact generates a spin accumulation at the Pt|YIG interface, which injects magnons into YIG. The latter diffuse into the magnet and when reaching another Pt contact generate a voltage  $V$  by the inverse spin Hall effect. The non-local resistance  $R_{nl} = V/I$  can be modulated by a third Pt film, as demonstrated for a 210 nm thick YIG film [9]. This three terminal device is a magnon transistor. The left and right ones inject and detect magnons thus form a *source* and a *drain*, respectively. Sending a current through the middle strip or *gate* modulate the source-drain signal by the magnon density in the transport channel.

Chumak et al. [10] achieved magnon transistor action by controlling the magnon scattering in a magnonic crystal by a magnetic field. Our device operates by modulating the magnon conductivity of a YIG thin film  $\sigma_m$  electrically. Similar to the Drude formula for electrons,

the magnon conductivity

$$\sigma_m = \hbar \frac{n_m \tau_m}{m_m}, \quad (1)$$

on the magnon density  $n_m$ , where  $\tau_m$  is the scattering time and  $m_m = \hbar^2/(2J_s)$  is the effective mass that is governed by the spin wave stiffness  $J_s$ .

The present study is motivated by the wish to improve the modulation efficiency of the previous device [9]. This can be achieved simply by a thinner YIG film, since for the same number of injected magnons, the magnon density in the source-drain transport channel should be larger [11]. To this end we grew an ultra-thin YIG film by liquid-phase epitaxy with thickness of 10 nm with great care in order to not sacrifice the low Gilbert damping of the thicker film. The observed modulation of the non-local signal reaches 200% corresponding to a modulation efficiency per DC current unit exceed 40%/mA, which is 20 times larger than for the 210 nm YIG [9]. A similar enhancement has been reported for a 13 nm thick YIG film grown by pulsed laser deposition and larger Gilbert damping [11]. The authors interpret an observed non-linearity in the gate-current dependence in terms of a diverging magnon conductivity by a spin Hall current-induced antidamping of the magnetization dynamics under the gate. Based on the observed dependence of the modulation on the gate width and geometry we believe that the physics is more complicated.

This paper is organized as follows: Section II addresses the device configuration, fabrication details and measurement methods. In Section III, we first compare the non-local signals in 10 nm and 210 nm thick YIG films. We then discuss the non-linearities that in contrast to the previous report [11] saturate, discuss other device configurations, and show results of spin Hall magnetoresistance

<sup>\*</sup> x.wei@rug.nl

<sup>†</sup> b.j.van.wees@rug.nl

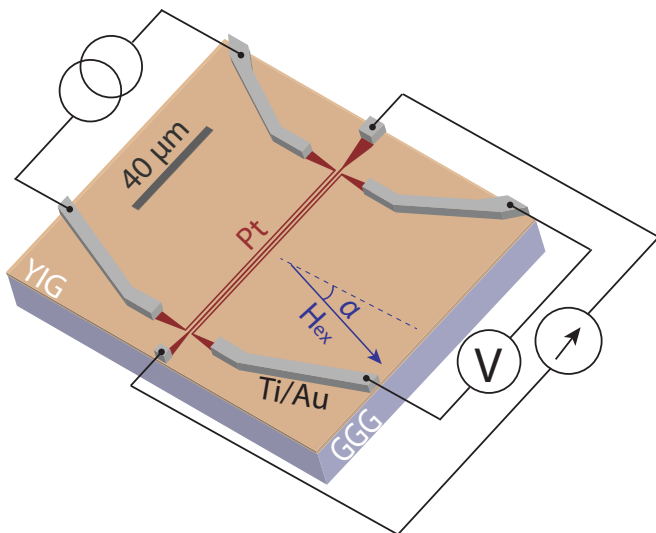


FIG. 1. Sample schematic: A 10 nm YIG film grown epitaxially on top of a GGG substrate. The sputtered Pt (red) strips with thickness of 9 nm are contacted by Ti/Au leads (grey). A low-frequency AC current with rms value of  $I_{ac}$  in the left Pt strip injects magnons. We measure both the first and second harmonic voltages over the right Pt strip by a lock-in technique. The DC current through the middle Pt middle gate modulated the source-drain signal. An external magnetic field  $H_{ex}$  orients the in-plane YIG magnetization at an angle  $\alpha$ . The dark-grey rectangle is a 40  $\mu\text{m}$  scale bar. Typically,  $\mu_0 H_{ex} = 50 \text{ mT}$ .

measurements of the Pt|YIG interface at high gate currents. In Section III, we compare our results with those reported by Wimmer et al. [11].

## II. EXPERIMENTAL DETAILS

The magnon transistors as depicted in Fig. 1 are fabricated on 10 nm thick single crystal yttrium iron garnet (YIG) films. The film is grown by liquid phase epitaxy (LPE) on top of a 500  $\mu\text{m}$  thickness single crystal (110) gadolinium gallium garnet (GGG,  $\text{Gd}_3\text{Ga}_5\text{O}_{12}$ ) substrate at the Université de Bretagne Occidentale in Brest, France. The saturation magnetization is  $\mu_0 M_s = 174 \pm 4 \text{ mT}$ . The Gilbert damping parameter of the in-plane magnetized film is  $\alpha_G = 5.2 \times 10^{-4}$ . All Pt strips, including the magnon injector, modulator and detector, are sputtered with thickness of 9 nm, patterned by electron beam lithography. Ti|Au layers with thicknesses of 5|75 nm are deposited by e-beam evaporation. The center-to-center distance between the injector and detector is 3  $\mu\text{m}$ . The length and width of the Pt strips for 3 measured devices are listed in Table I, but we focus on Device 1. Results for a fourth device with 7.9 nm thickness YIG are summarized in Appendix B. The sample is positioned between a pair of magnetic poles and rotated by a step motor. The magnetic field  $\mathbf{H}_{ex}$  orients the soft magnetization  $\mathbf{M}_0 \parallel \mathbf{H}_{ex}$  in the film plane at an angle  $\alpha$

TABLE I. Dimensions of the injector/modulator/detector Pt strips and selected observations. The centers of injectors and detectors are separated by 3  $\mu\text{m}$  and the Pt film thicknesses is 9 nm in all samples

Device	1	2	3
Length ( $\mu\text{m}$ )	80/84/80	20/24/20	20/24/20
Width ( $\mu\text{m}$ )	0.4/0.4/0.4	0.4/0.8/0.4	0.4/1.2/0.4
$I_{ac}$ ( $\mu\text{A}$ )	200	500	500
$I_{dc}$ (mA)	-1.5~1.5	-2.0~2.0	-2.25~2.25
$R_{nl}^{1\omega}$ at $I_{dc}=0$ ( $\Omega/\text{m}$ )	198	1044	160
Modulation efficiency (%/mA)	40.4	87	75

with respect to the Pt strips as shown in Fig. 1.

A low-frequency AC current through the magnon injector with an rms-amplitude of  $I_{AC}$ , thereby injecting magnons electrically and thermally. The resulting magnon spin currents are measured as the first and second harmonic signals at the magnon detector with a lock-in technique, respectively. A DC current  $I_{DC}$  is applied to the gate in order to modulate the magnon spin conductivity and the corresponding nonlocal signals.

The observed angle-dependent first harmonic signals of Device 1 are shown in Fig. 2: Colors, from red to blue code the nonlocal signals recorded for  $I_{DC}$  from -1500  $\mu\text{A}$  to +1500  $\mu\text{A}$ . The white dataset in the center for  $I_{DC} = 0$  has a typical  $\cos^2 \alpha$  dependence, i.e. the product of injection and detection efficiencies [8]. The DC bias modulates the magnitude and the angle dependence much more prominently than for a 210 nm thick YIG film [9], especially at the largest currents of  $-/+1500 \mu\text{A}$  (the darkest red/blue) and  $\alpha \approx 0$  and  $\alpha \approx \pm\pi$ . The gate annihilates magnons in YIG when the spin accumulation is parallel to the magnetic field but creates them when antiparallel, suppression and enhancing  $R_{nl}^{1\omega}$  is suppressed, respectively. The DC current enhances the signal by more than a factor of 2. Also the second harmonic signals are strongly modulated by the gate current (not shown), but more difficult to interpret since depending not only on the magnon density but also on the temperature profiles in the magnet. We therefore do not discuss them here.

## III. RESULTS AND DISCUSSION

### A. Dependence of the nonlocal signals on YIG film thickness

The nonlocal signals for 10 nm (Device 1 in Table I) and 210 nm thick YIG films with the same injector-to-

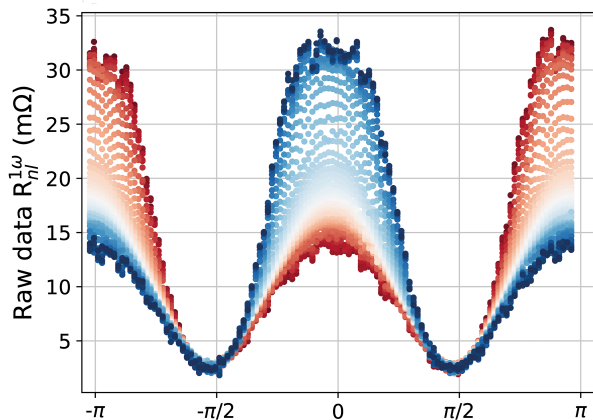


FIG. 2. Angle dependent  $R_{nl}^{1\omega}$ . Raw data of the first harmonic signals  $R_{nl}^{1\omega}$  at different DC gate currents with offset from inductive/capacitive coupling (at  $\alpha = \pm\pi/2$ ). The color gradient from red to blue represents DC currents from  $-1500 \mu\text{A}$  to  $+1500 \mu\text{A}$  with a step size of  $50 \mu\text{A}$ .

detector distance ( $3 \mu\text{m}$ ) are compared in Table II. The nonlocal resistances scale with the length of the Pt strips. The ultra-thin gated but unbiased  $10 \text{ nm}$  YIG sample shows a larger non-local signal than the thick one without gate, even though a passive central gate is a spin sink. This result is consistent with the thickness-dependence reported for films from  $100 \text{ nm}$  up to  $50 \mu\text{m}$  [12], but counterintuitive since a thinner film should have a higher impedance. It cannot be explained by either the magnon chemical potential model [13] nor viscous magnon flow [14]. On the other hand, the second harmonic spin Seebeck signal in  $10 \text{ nm}$  thick YIG (not shown) is much smaller in the  $10 \text{ nm}$  than in the  $210 \text{ nm}$  film. The thickness dependence of the nonlocal magnon transport remains unexplained. We may speculate for example about the existence of highly efficient surface transport channels that dominate in ultra thin films. The thickness dependence of the nonlocal signal will be discussed in a future paper with more details.

TABLE II. Comparison of the first-harmonic nonlocal signals in  $10 \text{ nm}$  and  $210 \text{ nm}$  thick YIG films.

YIG thickness (nm)	10	210[8]
$R_{nl}^{1\omega}$ ( $\Omega\text{m}^{-1}$ )	198	140
$R_{nl}^{2\omega}$ ( $\text{MVA}^{-2}\text{m}^{-1}$ )	0.09	1.35

## B. Saturation in the injector/modulator/detector geometry for a $400 \text{ nm}$ wide gate

The nonlocal resistances  $R_{nl}^{1\omega}$  are trigonometric functions of the magnetic field angle  $\alpha$  that reflect the electrical magnon injection and detection efficiencies [8]. The angle-dependent first-harmonic nonlocal resistances are well described by

$$R_{nl}^{1\omega}(\alpha) = C_1 \sigma_m^{1\omega}(\alpha) \cos^2 \alpha, \quad (2)$$

where  $C_1$  is a charge-spin conversion efficiency parameter of the electric spin injection and detection. In the limit of weak excitation, the magnon spin conductivity depends linearly on the magnon density which is again proportional to the injection current. We also include a quadratic term that does not depend on the current direction and is caused by Joule heating. Hence

$$\sigma_m^{1\omega}(\alpha) = \sigma_m^0 + \Delta\sigma_{\text{SHE}} I_{\text{DC}} \cos \alpha + \Delta\sigma_{\text{J}} I_{\text{DC}}^2, \quad (3)$$

where  $I_{\text{DC}}$  is the DC current in the modulator,  $\sigma_m^0$  is the magnon spin conductivity at thermal equilibrium,  $\Delta\sigma_{\text{J}}$  and  $\Delta\sigma_{\text{SHE}}$  are parameters that can be fitted to the observations.

We extract the non-local resistances at specific angles from Fig. 2 as a function of  $I_{\text{DC}}$ , subtracting a constant offset at  $\alpha = \pm\pi/2$  from the measured  $R_{nl}^{1\omega}(\alpha)$  that is caused by inductive/capacitive coupling. The signals at the angles  $\alpha = 0, \pm\pi$  are shown in Figs. 3a as well as normalized ones for  $\alpha = 0, \frac{\pi}{12}, \frac{\pi}{6}, \frac{\pi}{4}$  and  $\frac{\pi}{3}$  in Figs. 3b. When  $|I_{\text{DC}}| < I'_{\text{DC}} = 400 \mu\text{A}$  (The current density is  $1.1 \times 10^{11} \text{ A/m}^2$ ),  $R_{nl}^{1\omega}(\alpha)$  in Figs. 3a is to a good approximation a parabolic function of  $I_{\text{DC}}$ :

$$R_{nl}^{1\omega}(I_{\text{DC}}) = \mathcal{P}_0^{1\omega} + \mathcal{P}_1^{1\omega} I_{\text{DC}} + \mathcal{P}_2^{1\omega} I_{\text{DC}}^2, \quad (4)$$

with  $\mathcal{P}_1^{1\omega} \sim 6 \Omega/\text{A}$  and  $\mathcal{P}_2^{1\omega} \sim 5 \times 10^3 \Omega/\text{A}^2$  ( $\mathcal{P}_0^{1\omega} = 1$  for the normalized data in Figs. 3b). The differences between the observations and the fits of Figs. 3a/b are given in Figs. 3c/d, respectively. The data deviate from the fits at the first threshold current  $|I_{\text{DC}}| \gtrsim I'_{\text{DC}} = 400 \mu\text{A}$  (current density  $1.1 \times 10^{11} \text{ A/m}^2$ ). At a second threshold  $I''_{\text{DC}} = 800 \mu\text{A}$  (current density  $2.2 \times 10^{11} \text{ A/m}^2$ ) the deviations from the polynomial fits show a *maximum* that we call an *anomaly* for convenience. For  $I_{\text{DC}} < 0$  the parabolic model Eq. (3) predicts an increase of the magnon conductivity by the parabolic term that models the magnon injection by Joule heating. However,  $R_{nl}^{1\omega}(0)$  deviates from this prediction for  $I_{\text{DC}} \lesssim -I'_{\text{DC}}$ , i.e. at the same current level as for positive gate currents. The experiments confirm that reversing the magnetic field is equivalent to reversing the current direction. The threshold  $I''_{\text{DC}}$  in Fig. 3d increases with the angle  $\alpha$ , while  $I'_{\text{DC}}$  remains constant. Since with increasing  $\alpha$  a higher current is required to inject the same number of magnons,  $I''_{\text{DC}}$  appears to be related with the magnon injection process, while  $I'_{\text{DC}}$  is not.

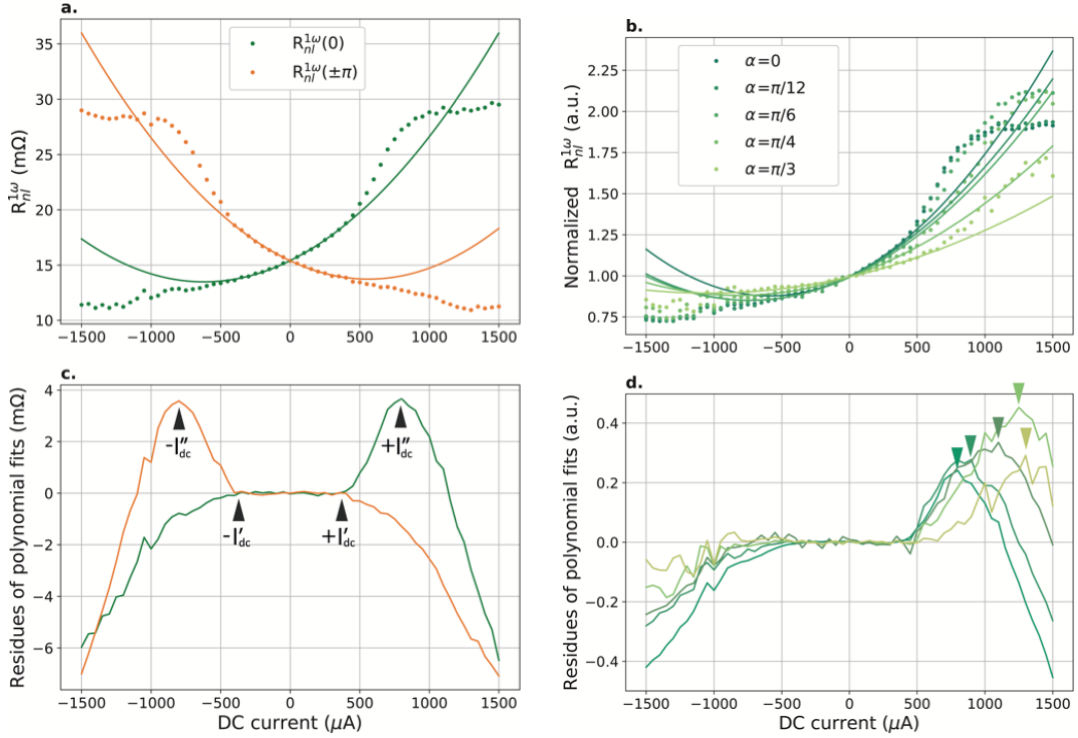


FIG. 3. Analysis of  $R_{\text{ni}}^{1\omega}$  at specific angles  $\alpha$  for Device 1. The dots are the experimental data and the lines with the same color are quadratic fits for small currents. a.  $\bullet R_{\text{ni}}^{1\omega}(0)$  and  $\alpha + \phi^{1\omega} = \pm\pi$  ( $\circ R_{\text{ni}}^{1\omega}(\pm\pi)$ ) as a function of DC gate current  $I_{\text{DC}}$ . b. Data for  $\alpha = \{0, \pi/12, \pi/6, \pi/4, \pi/3\}$  normalized by the amplitudes at  $I_{\text{DC}} = 0$  (green dots with different brightness). The deviations from the fits in a. and b. are plotted in c. and d., respectively.

### C. External field dependence of the saturation

A field-dependent study can shed light on the possible effect of the magnon gap or Kittel frequency

$$\omega_{k=0} = \gamma \sqrt{B_0 (B_0 + \mu_0 M_s)}, \quad (5)$$

on the anomaly  $I_{\text{DC}}''$ . The results in Fig. 4 show a slightly increased  $I_{\text{DC}}''$  with field from  $700 \mu\text{A}$  to  $1 \text{mA}$ . This could reflect a gap-induced reduction of the magnon number and conductivity.  $I_{\text{DC}}'$ , which we found to not depend on the magnetization angle above, remains also resilient against the magnetic field strength, however.

### D. Spin Hall magnetoresistance of the 400 nm wide Pt strip

Next, we analyze the spin Hall magnetoresistance (SMR) of the 400 nm wide Pt center gate [15] for an AC current of  $20 \mu\text{A}$  and a DC current range from  $-590 \mu\text{A}$  to  $590 \mu\text{A}$ . Fig. 5 shows that the resistance change  $\Delta R$  decreases with DC current  $I_{\text{DC}}$  with a threshold around  $\pm 400 \mu\text{A}$ , close to  $I_{\text{DC}}'$  introduced above. Since the SMR decreases with temperature [16] and appears to be correlated with  $I_{\text{DC}}'$ , the first threshold in the non-local signal could be heat-induced, consistent with its independence on the magnetic field reported above.

### E. Exchanged source and gate contacts

In order collect more information on the anomalies observed in Figs. 3 we exchange roles of the Pt contacts from an injector/modulator/detector to a modulator/injector/detector geometry in Device 1 as sketched in Figs. 6b and specified in Table III. In this configuration the source-drain current is not directly affected by an antidamping torque of the modulator. The signal is larger because the injector and detector are now closer to each other. The first harmonic signal for the new configuration in Fig. 7 is well represented by a parabola with  $\mathcal{P}_1^{1\omega} \sim 1.6 \times 10^{-2} \Omega/\text{A}$  and  $\mathcal{P}_2^{1\omega} \sim 18 \Omega/\text{A}^2$  in Eq. (4) for  $|I_{\text{DC}}| < I_{\text{DC}}' = 900 \mu\text{A}$ .  $R_{\text{ni}}^{1\omega}(0)$  ( $R_{\text{ni}}^{1\omega}(\pm\pi)$ ) start to decrease for at currents  $I_{\text{DC}} = 900 \mu\text{A}$  ( $1400 \mu\text{A}$ ) and  $I_{\text{DC}} = -1400 \mu\text{A}$  ( $-900 \mu\text{A}$ ). In contrast to the discussion above, the deviations from the parabolic fit at  $I_{\text{DC}}'$  are negative so we cannot identify a  $I_{\text{DC}}''$ .

In the modulator/injector/detector geometry, magnons injected by the modulator first have to diffuse to the region between the injector and detector in order to affect the magnon conductivity. The magnon chemical potential  $\mu_{\text{m}}$  is a direct measure of the non-equilibrium magnon density that obeys the spin diffusion equation  $d^2 \mu_{\text{m}}/dx^2 = \mu_{\text{m}}/\lambda_{\text{m}}^2$  [8] with a magnon diffusion length of  $\lambda_{\text{m}} \sim 10 \mu\text{m}$  at room temperature. The magnon density in the source-drain channel amounts of

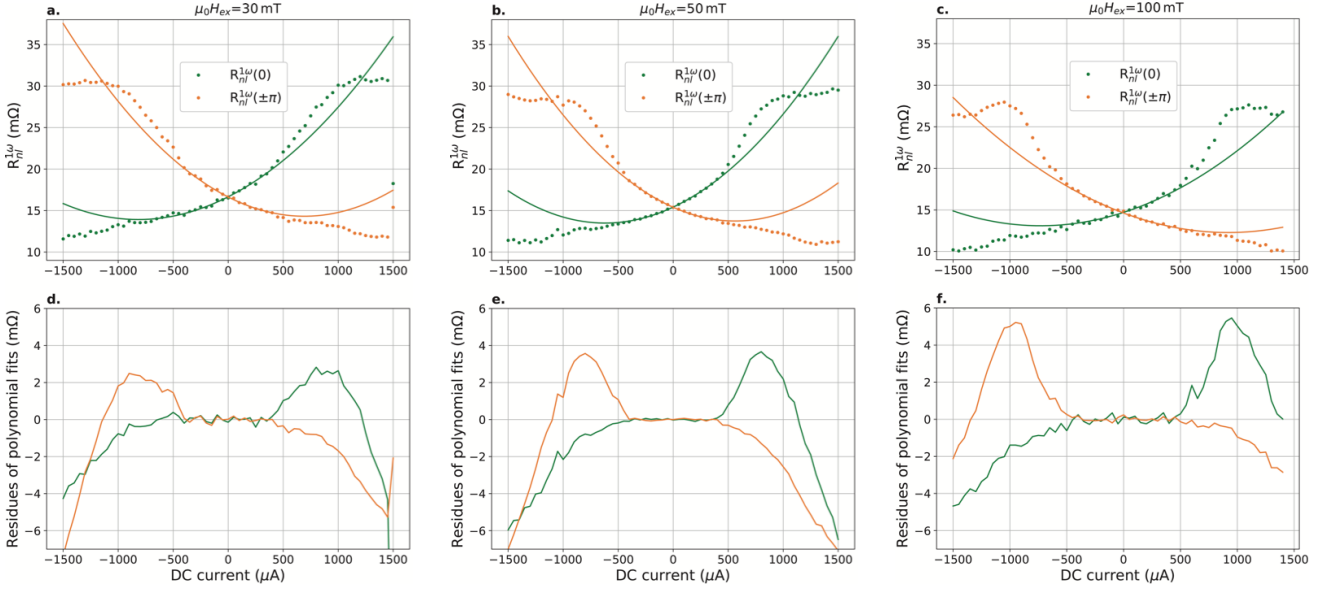


FIG. 4. Analysis of the non-parabolicities in  $R_{nl}^{1\omega}$  of Device 1 for different magnetic field. We plot the deviations from the small-field parabolic fits for  $\alpha = 0$  ( $\bullet R_{nl}^{1\omega}(0)$ ) and  $\alpha = \pm\pi$  ( $\bullet R_{nl}^{1\omega}(\pm\pi)$ ) as a function of the modulator current  $I_{DC}$  at 30 mT, b 50 mT and c 100 mT.

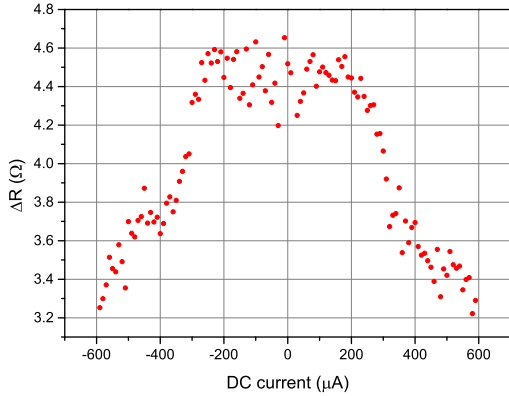


FIG. 5. (Longitudinal) spin Hall magnetoresistance of the 400 nm wide central Pt gate at DC current from  $-590 \mu\text{A}$  to  $590 \mu\text{A}$ .

the side-modulator geometry should be reduced to about 80% of the value for the center gate configuration. A larger current must therefore be applied to achieve the same magnon density. The additional heating may explain the reduced performance.

#### F. Modulator gate width dependence

In Device 2 (800 nm wide modulator) and Device 3 (1200 nm wide modulator) from Table I (see Fig. 8), a saturation as in Device 1 (Fig. 3a) is not observed. The characteristics are similar to that of Device 1 in the

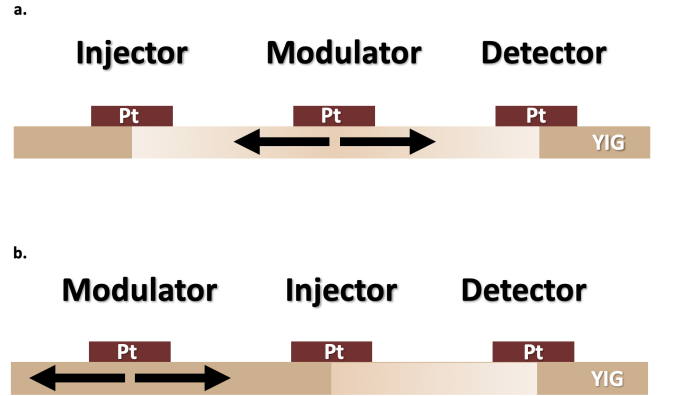


FIG. 6. The position of the modulating gate in two different configurations. The black arrows represent the diffusion current of the magnons injected by the modulator, while the lighter shaded regions indicate the source-drain path. a. injector/modulator/detector configuration and b. modulator/injector/detector configuration.

modulator/injector/detector configuration:  $R_{nl}^{1\omega}$  deviates from the simple magnon conductivity model at lower currents. Device 2 deviates at currents (current densities) of  $500 \mu\text{A}$  ( $0.7 \times 10^{11} \text{ A/m}^2$ ) and starts to decrease at  $1 \text{ mA}$  ( $1.4 \times 10^{11} \text{ A/m}^2$ ). Device 3 deviates from  $0.6 \times 10^{11} \text{ A/m}^2$  and starts to decrease at  $1.2 \times 10^{11} \text{ A/m}^2$ . They are much lower than the current density corresponding to the saturation in Device 1 ( $2.2 \times 10^{11} \text{ A/m}^2$ ). How the width of the gate affects the nonlinear effect also needs further investigation.

We also observe signal changes induced by a high DC

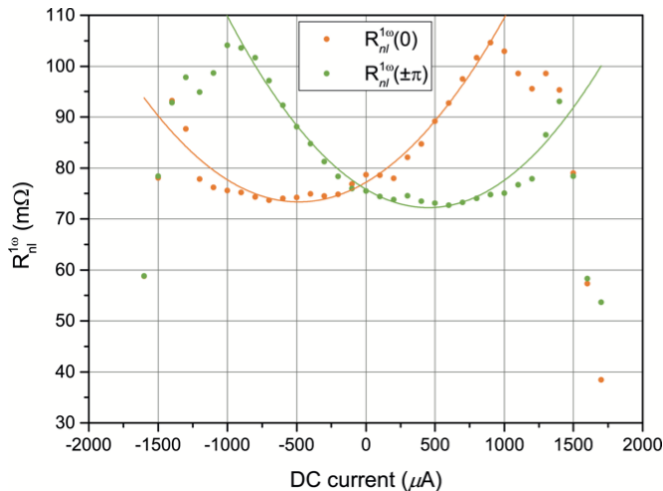


FIG. 7. Analysis of  $R_{nl}^{1\omega}$  at specific angles for modulator/injector/detector configuration. Relative amplitudes of the first harmonic nonlocal signals of device 2 with 800 nm width modulator at  $\alpha = 0$  ( $\bullet R_{nl}^{1\omega}(0)$ ) and  $\alpha = \pm\pi$  ( $\bullet R_{nl}^{1\omega}(\pm\pi)$ ) as a function of dc currents.

TABLE III. Geometry of modulator/injector/detector Pt strips and measurement parameters.

Length ( $\mu\text{m}$ )	20/24/20
Width ( $\mu\text{m}$ )	0.4/0.8/0.4
Pt thickness (nm)	9
$I_{ac}$ ( $\mu\text{A}$ )	500
$I_{dc}$ (mA)	-1.6~1.7
Modulation efficiency (%/mA)	23.5

current bias on Device 3 (see Appendix A) that indicate a transient change of the magnetic order of the YIG film that may also cause the asymmetry between the data in Fig. 8 for flipped current and magnetization directions. Rather than blowing the sample up, we observed a strong increase of the non-local signals. Since we have not been able to explain or repeat these results we do not discuss them in the main text.

#### IV. DISCUSSION AND CONCLUSIONS

We report large modulations of nonlocal magnon transport in a 10 nm thick YIG film by a DC current through a Pt gate. For the injector/modulator/detector geometry, a threshold current  $I'_{DC}$  separates the low and high DC current regimes. The enhancement of the magnon transport at currents  $I > I'_{DC}$  indicates interesting physics such as current-induced self-oscillations of the magnetic

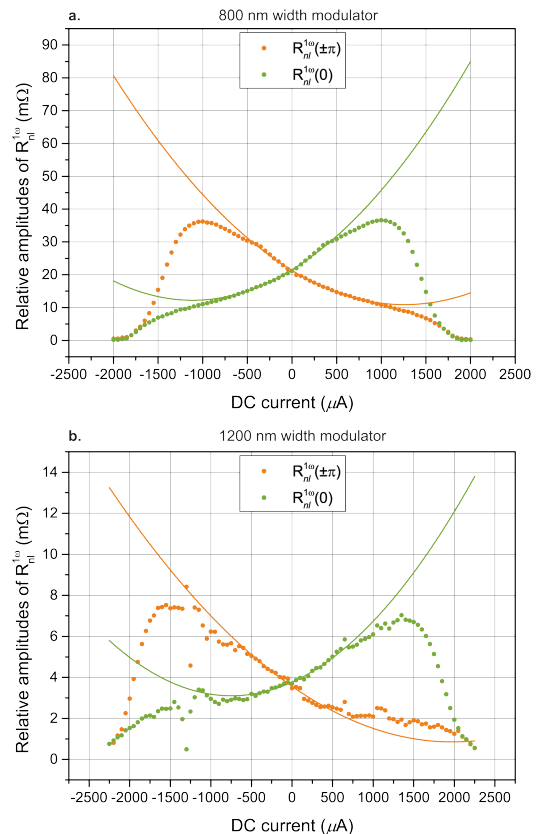


FIG. 8.  $R_{nl}^{1\omega}$  for Devices 2 and 3 with wider modulator gates as a function of gate current  $I_{DC}$ . a. The signals of Device 2 with 800 nm wide modulator at  $\alpha = 0$  ( $\bullet R_{nl}^{1\omega}(0)$ ) and  $\alpha = \pm\pi$  ( $\bullet R_{nl}^{1\omega}(\pm\pi)$ ) as a function of dc currents. b. As a function of gate current  $I_{DC}$ , but for Device 3 with 1200 nm wide modulator.

order. However, instead of a divergence that could indicate magnon superfluidity, we observe a plateau at high current levels Figs. 3a.

The differences between the data and a parabolic fit at low injection currents sheds some light on what is happening. We clearly observe non-parabolicities for both positive and negative currents, i.e. for both magnon injection and extraction. At  $I > I'_{DC}$  the signal is enhanced, i.e. increases above the parabolic fit. This threshold is not sensitive to applied magnetic fields and angles, which indicates a thermal (spin Seebeck) mechanism for the enhancement of the conductivity as reported by C. Safranski et al. [17]. The SMR data are suppressed around  $I'_{DC}$ , thereby supporting the hypothesis that Joule heating affects the spin-transport at the interface. The residue of the polynomial fit in Figs. 3c shows a maximum, i.e. a peak at the threshold current  $I'_{DC}$  (in one current direction), and then decreases again. We cannot pinpoint the process that suppresses the magnon conduction at high current levels to a certain mechanism, but it appears to be spin-dependent since in contrast to  $I'_{DC}$ ,  $I''_{DC}$  depends

strongly on the magnetic field strength and direction.

When the modulator is in the center, the magnon transmission is affected by thermal [18, 19] or electric [20, 21] spin-orbit torques as well as spin absorption by the Pt gate. The situation is simplified for the modulator/injector/detector geometry in so far that the modulator is only a source of additional magnons that increase the injector-detector conductance.  $I'_{DC}$  is larger for this configuration, presumably because the higher current level is required to generate the same density in the source-drain channel by magnon diffusion. However, in contrast to the center-gate configuration, the signal always stays under the parabolic fit. This indicates that the magnon density is not the only parameter relevant for magnon transport, confirming that a spin Seebeck torque from the Pt interface plays an essential role.

Naively, we expected that for equal current densities the results should not depend on the width of the gate. Nevertheless we find that widening the central gates only decreases the signals relative to the polynomial fit. A proper explanation of this result requires more research.

Summarizing, we observe a threshold behavior at currents  $I > I'_{DC}$  that indicates that the film under the gate approaches an instability, confirming previous reports. The threshold does not depend on the magnetization direction and therefore the spin Hall injection, which could indicate an enhancement of the magnon density by the spin Seebeck effect. However, at negative currents the magnon accumulation remains suppressed which indicates that the spin Hall effect injection dominates the spin Seebeck effect. At even higher currents  $I \gtrsim I''_{DC}$  another effect kicks in that suppresses the magnon density and conductivity again. This process is roughly symmetric in the current direction and may be assigned to a non-linear magnon decay into phonons at elevated temperatures.

Wimmer et al. [11] also report non-linear effects induced by a Pt gate current on magnon transport. Their sample is slightly thicker with 13.5 nm with a damping of  $\alpha_G = 2.17 \times 10^{-3}$  which is significantly higher than our  $\alpha_G = 5.2 \times 10^{-4}$ . They report two anomalies ( $I_{on}$  and  $I_{crit}$ ). The first appears to agree with our  $I'_{DC}$  and results for  $I_{DC} < I'_{DC}$  agree qualitatively with our data and the magnon conductivity Eq. (3). The current densities correspond to  $I_{on}$  ( $3.2 \times 10^{11}$  A/m<sup>2</sup>) and

$I_{crit}$  ( $4.3 \times 10^{11}$  A/m<sup>2</sup>) are much higher than our  $I'_{DC}$  ( $1.1 \times 10^{11}$  A/m<sup>2</sup>) and  $I''_{DC}$  ( $2.2 \times 10^{11}$  A/m<sup>2</sup>). They do not report transport for opposite gate current direction and the associated suppression of the non-local signals, however. For  $I_{DC} > I_{on}$ , Wimmer et al. [11] observe signals that increases faster than the parabolic fit, which we confirm here. However, they do not find the saturation we report in Figs. 3a. Wimmer et al. [11] interpret the monotonic increase of their results as an incipient divergence by an anti-damping spin-orbit torque that compensates the damping in the YIG film under the gate and speculate about lossless magnon transport at the onset of self-oscillations or superfluidity. On the other hand, the larger Gilbert damping in their samples could imply that the magnon densities at their highest current levels is significantly lower than ours, so they do not reach the saturation regime that we report here.

Concluding, before drawing conclusion about the nature of nonlinearities, the complications due to heating should be figured out in more detail [22–25]. It would be valuable to assess the magnon spin accumulation profile governed by the temperature gradient [26], which may be different in thin and thick films. We conclude that ultrathin YIG films are a great platform for the research on magnon transport in nonlinear regime, but much work has still to be carried out before magnon Bose-Einstein condensation or superfluidity by electric or thermal spin injection can be confirmed.

## V. ACKNOWLEDGMENTS

We acknowledge the helpful discussion with T. Yu and technical support from J. G. Holstein, H. M. de Roos, H. Adema T. Schouten and H. de Vries. This work is part of the research program Magnon Spintronics (MSP) No. 159 financed by the Foundation for Fundamental Research on Matter (FOM), which is part of the Netherlands Organisation for Scientific Research (NWO), and supported by the research programme Skyrmionics with project number 170, which is financed by the Dutch Research Council (NWO). The support by NanoLab NL is also gratefully acknowledged. G.B. was supported by JSPS Kakenhi Grant 19H006450.

- 
- [1] A. V. Chumak, V. I. Vasyuchka, A. A. Serga, and B. Hillebrands, *Nature Physics* **11**, 453 (2015).
  - [2] C. Kittel, *Phys. Rev.* **110**, 1295 (1958).
  - [3] J. R. Eshbach, *Phys. Rev. Lett.* **8**, 357 (1962).
  - [4] R. Lebrun, A. Ross, S. A. Bender, A. Qaiumzadeh, L. Baldrati, J. Cramer, A. Brataas, R. A. Duine, and M. Kläui, *Nature* **561**, 222 (2018).
  - [5] K. Oyanagi, S. Takahashi, L. J. Cornelissen, J. Shan, S. Daimon, T. Kikkawa, G. E. W. Bauer, B. J. van Wees, and E. Saitoh, *Nature Communications* **10**, 4740 (2019).
  - [6] K. Uchida, S. Takahashi, K. Harii, J. Ieda, W. Koshihara, K. Ando, S. Maekawa, and E. Saitoh, *Nature* **455**, 778 (2008).
  - [7] Y. Kajiwara, K. Harii, S. Takahashi, J. Ohe, K. Uchida, M. Mizuguchi, H. Umezawa, H. Kawai, K. Ando, K. Takanashi, S. Maekawa, and E. Saitoh, *Nature* **464**, 262 (2010).
  - [8] L. J. Cornelissen, J. Liu, R. A. Duine, J. Ben Youssef, and B. J. van Wees, *Nature Physics* **11**, 1022 (2015).

- [9] L. J. Cornelissen, J. Liu, B. J. van Wees, and R. A. Duine, *Phys. Rev. Lett.* **120**, 097702 (2018).
- [10] A. V. Chumak, A. A. Serga, and B. Hillebrands, *Nature Communications* **5**, 4700 (2014).
- [11] T. Wimmer, M. Althammer, L. Liensberger, N. Vlietstra, S. Geprägs, M. Weiler, R. Gross, and H. Huebl, *Phys. Rev. Lett.* **123**, 257201 (2019).
- [12] J. Shan, L. J. Cornelissen, N. Vlietstra, J. Ben Youssef, T. Kuschel, R. A. Duine, and B. J. van Wees, *Phys. Rev. B* **94**, 174437 (2016).
- [13] L. J. Cornelissen, K. J. H. Peters, G. E. W. Bauer, R. A. Duine, and B. J. van Wees, *Phys. Rev. B* **94**, 014412 (2016).
- [14] C. Ulloa, A. Tomadin, J. Shan, M. Polini, B. J. van Wees, and R. A. Duine, *Phys. Rev. Lett.* **123**, 117203 (2019).
- [15] Y. Chen, D. Roy, E. Cogulu, H. Chang, M. Wu, and A. D. Kent, *Applied Physics Letters* **113**, 202403 (2018), <https://doi.org/10.1063/1.5053120>.
- [16] S. Vélez, A. Bedoya-Pinto, W. Yan, L. E. Hueso, and F. Casanova, *Phys. Rev. B* **94**, 174405 (2016).
- [17] C. Safranski, I. Barsukov, H. K. Lee, T. Schneider, A. A. Jara, A. Smith, H. Chang, K. Lenz, J. Lindner, Y. Tserkovnyak, M. Wu, and I. N. Krivorotov, *Nature Communications* **8**, 117 (2017).
- [18] E. Padrón-Hernández, A. Azevedo, and S. M. Rezende, *Phys. Rev. Lett.* **107**, 197203 (2011).
- [19] S. A. Bender and Y. Tserkovnyak, *Phys. Rev. B* **93**, 064418 (2016).
- [20] A. Hamadeh, O. d'Allivy Kelly, C. Hahn, H. Meley, R. Bernard, A. H. Molpeceres, V. V. Naletov, M. Viret, A. Anane, V. Cros, S. O. Demokritov, J. L. Prieto, M. Muñoz, G. de Loubens, and O. Klein, *Phys. Rev. Lett.* **113**, 197203 (2014).
- [21] M. Collet, X. de Milly, O. d'Allivy Kelly, V. V. Naletov, R. Bernard, P. Bortolotti, J. Ben Youssef, V. E. Demidov, S. O. Demokritov, J. L. Prieto, M. Muñoz, V. Cros, A. Anane, G. de Loubens, and O. Klein, *Nature Communications* **7**, 10377 (2016).
- [22] N. Thiery, V. V. Naletov, L. Vila, A. Marty, A. Brenac, J.-F. Jacquot, G. de Loubens, M. Viret, A. Anane, V. Cros, J. Ben Youssef, N. Beaulieu, V. E. Demidov, B. Divinskiy, S. O. Demokritov, and O. Klein, *Phys. Rev. B* **97**, 064422 (2018).
- [23] H. J. Qin, K. Zakeri, A. Ernst, and J. Kirschner, *Phys. Rev. Lett.* **118**, 127203 (2017).
- [24] S. Geprägs, A. Kehlberger, F. D. Coletta, Z. Qiu, E.-J. Guo, T. Schulz, C. Mix, S. Meyer, A. Kamra, M. Althammer, H. Huebl, G. Jakob, Y. Ohnuma, H. Adachi, J. Barker, S. Maekawa, G. E. W. Bauer, E. Saitoh, R. Gross, S. T. B. Goennenwein, and M. Kläui, *Nature Communications* **7**, 10452 (2016).
- [25] Y. Nambu, J. Barker, Y. Okino, T. Kikkawa, Y. Shiomi, M. Enderle, T. Weber, B. Winn, M. Graves-Brook, J. M. Tranquada, T. Ziman, M. Fujita, G. E. W. Bauer, E. Saitoh, and K. Kakurai, *Phys. Rev. Lett.* **125**, 027201 (2020).
- [26] J. Shan, L. J. Cornelissen, J. Liu, J. Ben Youssef, L. Liang, and B. J. van Wees, *Phys. Rev. B* **96**, 184427 (2017).

### Appendix A: Signal change after gate measurement

Device 3 underwent a transient change after applying a high DC current to the gate. The signal became sym-

metric around zero angle and enhanced for both 0 and 180 degrees, see Fig. 9, indicating an unidentified thermal mechanism. After this experiment, the nonlocal signal at zero gate current increased by a factor five as shown in Fig. 10. The high DC current appeared to change the properties of YIG under the gate. However, after about two weeks, the characteristics of Device 2 returned back to normal as shown in Fig. 8b.

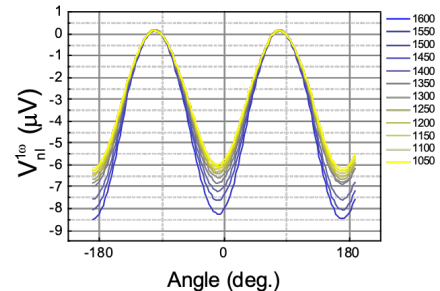


FIG. 9. Angle-dependent first harmonic voltages at high gate current levels. The nonlocal signal continues to increase with increasing current.

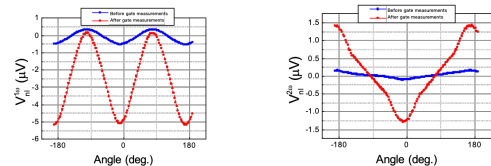


FIG. 10. Angle-dependent nonlocal magnon transport measurement before and after a measurement at high gate currents. The heating that accompanies a large current changes the properties of YIG. **a** Angle-dependent first harmonic voltage before and after the gate-induced heating at zero gate current. **b** Angle-dependent second harmonic measurement before and after. Both first and second harmonic signals are strongly enhanced after the heating. However, the effect appears to be transient and could not be reproduced.

### Appendix B: Modulation effect on 7.9 nm thick YIG

We also study a transistor structure on a 7.9 nm thick YIG with damping parameter of  $\alpha_G = 6.3 \times 10^{-4}$ . The device parameters are shown in Table IV. Compared to the 10 nm thick YIG, we observe in Fig. 11 a modulation increased by a factor of 3 instead of 2. We have to apply a higher DC currents to reach the nonlinear regime but still observe a saturation at the highest currents.



TABLE IV. Geometry of injector/modulator/detector Pt strips.

Length ( $\mu\text{m}$ )	20/25/20
Width ( $\mu\text{m}$ )	0.4/0.4/0.4
Pt thickness (nm)	8
$I_{\text{ac}}$ ( $\mu\text{A}$ )	200
$I_{\text{dc}}$ (mA)	-1.75~1.75
Distance between centers of Pt ( $\mu\text{m}$ )	1.5

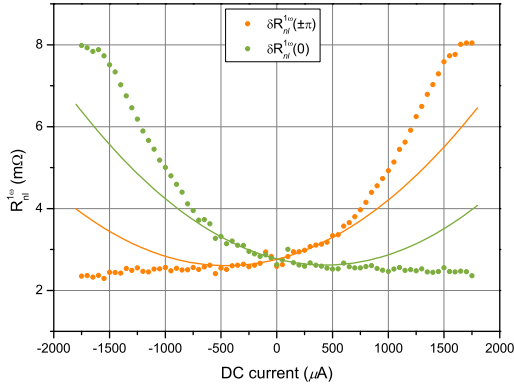


FIG. 11.  $R_{\text{nl}}^{1\omega}$  for modulator/injector/detector configuration for the 7.9 nm YIG film specified in Table IV. Relative amplitudes of the first harmonic nonlocal signals of device 2 with 800 nm width modulator at  $\alpha = 0$  ( $\bullet R_{\text{nl}}^{1\omega}(0)$ ) and  $\alpha = \pm\pi$  ( $\bullet R_{\text{nl}}^{1\omega}(\pm\pi)$ ) as a function of dc currents.